AlGaN-Based Self-Powered Solar-Blind UV Focal Plane Array Imaging Photosensors: Material Growth, Device Preparation, and Functional Verification

Yiren Chen, Xinye Fan, Zhiwei Zhang, Guoqing Miao, Hong Jiang, and Hang Song

***Abstract*—This article reports the development of hybrid AlGaN-based self-powered solar-blind ultraviolet (UV) focal plane array (FPA) imaging photosensors from material growth and array preparation to functional verification. The detailed process starts with the epitaxial growth by metal-organic chemical vapor deposition (MOCVD). A high-quality AlN template is obtained on the 2-in double-polished *c*-plane sapphire substrate by introducing a mesothermal AlN (MT-AlN) interlayer and adjusting the growth rate of the high-temperature AlN epilayer (HT-AlN). Then, a polarization-enhanced p-i-n structure photodetector material is grown on the AlN template. Subsequently, based on the p-i-n structural material, a 320 × 256 back-illuminated solar-blind photodiode array is fabricated and hybridized to a matching Si-based CMOS readout integrated circuit (ROIC) chip to form a focal plane detector. Solar-blind UV detection is observed throughout the array in the 262–281-nm spectral region with a peak external quantum efficiency (EQE) of 65.3% at zero-bias voltage (no antireflection coating) and a nanosecond transient response time at a reverse bias of 5 V. The visible response of the ROIC is eliminated by developing a masking technology that is opaque to visible light, which enables the focal plane detector to achieve a high UV/visible rejection ratio of more than 10^4.**

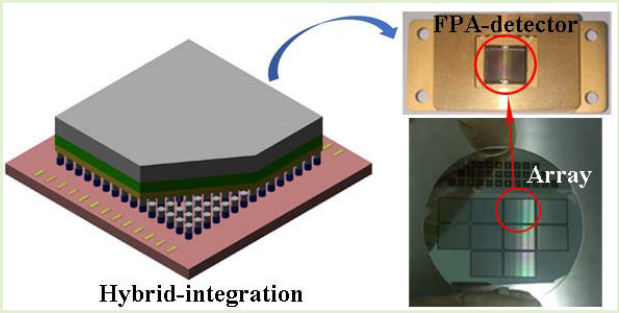

***Index Terms*— AlGaN, AlN template, focal plane array (FPA), gradient layer, metal-organic chemical vapor deposition (MOCVD), photodetector.**

I. Introduction

During the photoelectric detection process, solar radiation negatively affects the ability of the detector to capture target information. Fortunately, ozone in the stratosphere can filter out optical interference in the 200–280-nm band, forming a detection band near the ground without the background of solar radiation, called the solar-blind ultraviolet (UV) band [1], [2], [3]. Solar-blind UV photoelectric imaging sensors as optical signal receivers have essential applications in national defense and national economic construction, such as missile approach warning, early fire warning, leakage monitoring of ultrahigh voltage transmission lines, ozone concentration monitoring, and UV astronomy, especially in the emerging non-line-of-sight secure optical communication due to its pretty good privacy and anti-interference [4], [5], [6]. Driven by expansive application prospects, more and more emergent materials are used to develop solar-blind UV photosensors, typically such as group-III nitride alloy semiconductors [7], [8], oxide semiconductors [9], [10], 2-D semiconductors [11], [12], and ITO/Ag/ITO multilayer films [13]. It is worth noting that the group-III nitride alloy semiconductor $Al_xGa_{1-x}N$, with the advantages of direct wide bandgap, high optical absorption coefficient, and high chemical stability is considered to be an ideal material for developing high-

Manuscript received 12 February 2023; accepted 3 March 2023. Date of publication 10 March 2023; date of current version 14 September 2023. This work was supported in part by the Independent Project of State Key Laboratory of Luminescence and Applications under Grant SKLA-Z-2022-10 and in part by the National International Science and Technology Cooperation Project under Grant 2014DFR10910. The associate editor coordinating the review of this article and approving it for publication was Dr. Shahid Mumtaz. *(Corresponding authors: Yiren Chen; Hang Song.)*

Yiren Chen, Zhiwei Zhang, Guoqing Miao, Hong Jiang, and Hang Song are with the State Key Laboratory of Luminescence and Applications, Changchun Institute of Optics, Fine Mechanics and Physics, Chinese Academy of Sciences, Changchun 130033, China (e-mail: chenyr@ciomp.ac.cn; songh@ciomp.ac.cn).

Xinye Fan is with the State Key Laboratory of Luminescence and Applications, Changchun Institute of Optics, Fine Mechanics and Physics, Chinese Academy of Sciences, Changchun 130033, China, and also with the School of Optoelectronics, University of Chinese Academy of Sciences, Beijing 100049, China.

Digital Object Identifier 10.1109/JSEN.2023.3253724

performance self-powered solar-blind UV photosensors to satisfy the usage in the extreme environment such as high temperature, high humidity, strong radiation, and so on [14]. Moreover, the advantages of all-solid-state, small size, low power consumption, high reliability, and no need for a filter are also manifested in the AlGaN-based self-powered solar-blind UV focal plane array (FPA) imaging sensor.

This article reports the development of a hybrid AlGaN-based self-powered solar-blind UV FPA photosensor from material growth, array preparation, and hybrid integration to functional verification in detail, which has excellent reference significance for the manufacture of the AlGaN-based self-powered solar-blind UV imaging sensor. The whole process starts with the preparation of a high-quality, crack-free AlN epilayer on the 2-in double-polished *c*-plane sapphire substrate by metal-organic chemical vapor deposition (MOCVD), followed by the growth of polarization-enhanced p-i-n structure high Al content AlGaN photosensitive material. Using the p-i-n structural material, a 320 × 256 FPA of back-illuminated solar-blind photodiodes is fabricated by a standard photoelectronic process. For the purpose of eliminating the visible response of the readout integrated circuit (ROIC) caused by environmental visible light passing through the array pixel gaps, an opaque masking technology is developed, which enables the FPA to achieve a high UV/visible rejection ratio. Followed by hybridizing to a matching Si-based CMOS ROIC chip, the obtained FPA photosensor is characterized, and imaging verification is conducted to evaluate its performance. It is worth noting that its fast response time contributes to high-speed imaging capture.

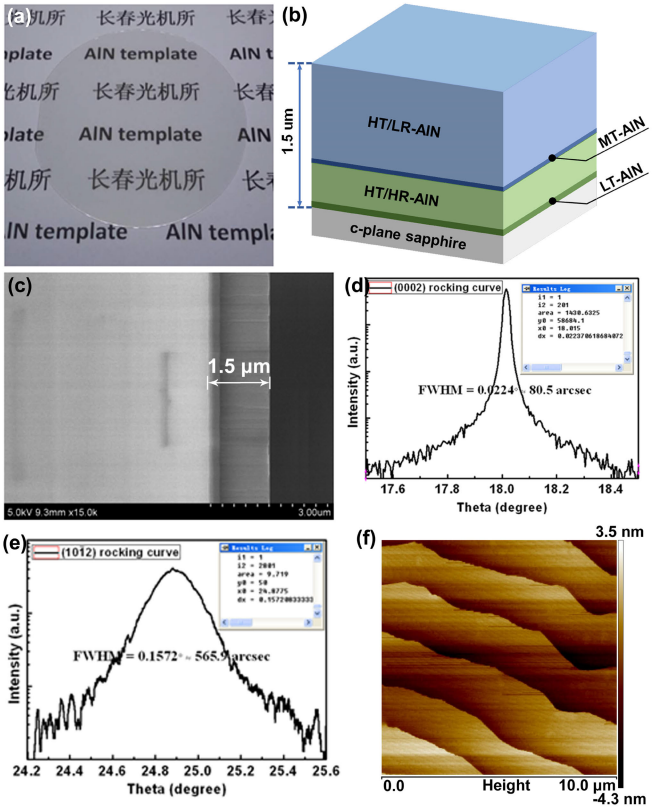

Fig. 1. AlN template as the substrate for AlGaN-based material growth. (a) 2-in AlN template. (b) Schematic of AlN template structure. (c) Cross-sectional SEM of AlN template. (d) (0002)-plane rocking curve. (e) (10$\bar{1}$2)-plane rocking curve. (f) AFM surface morphology of AlN.

II. Experimental Details

A. Material Growth

AlN template is considered to be an excellent substrate for the growth of AlGaN materials with high Al content, and its crystal quality determines that of subsequent solar-blind UV photodetector material [15], [16]. Therefore, prior to the growth of AlGaN-based p-i-n structural material, it is necessary to obtain high-quality AlN templates. Herein, a high-quality AlN template was grown on the 2-in double-sided polished *c*-plane sapphire substrate by introducing a mesothermal AlN (MT-AlN) interlayer and adjusting the growth rate of the high-temperature AlN epilayer (HT-AlN) using low-pressure MOCVD. Fig. 1(a) shows the physical image of a 2-in AlN template, which presents excellent transparency. During epitaxial growth, trimethylaluminum (TMAl) and ammonia (NH_3) are used as Al and N sources, respectively. To remove the surface contaminants and form the N-rich polar surface, the sapphire substrate is thermally desorbed at 1200 °C under mixed gas of hydrogen (H_2) and NH_3 [17]. Then, the AlN epilayer including a low-temperature AlN (LT-AlN) nucleation layer, a high-temperature/high growth rate AlN (HT/HR-AlN) layer, an MT-AlN interlayer, and a high-temperature/low growth rate AlN (HT/LR-AlN) layer is designed with a total thickness of 1.5 μm, as shown in Fig. 1(b). The LT-AlN nucleation layer is grown at 950 °C with a V/III ratio of about 2000. The MT-AlN interlayer is grown at 1050 °C with a V/III ratio of about 700. Both the HT/HR-AlN layer and the HT/LR-AlN layer are grown at 1280 °C. Through adjusting the V/III ratio, the former is grown at a rate of 0.31 nm/s, while the latter is grown at a rate of 0.12 nm/s.

Furthermore, material characterization has been carried out for the purpose of evaluating the quality of the AlN template, and relevant results have been obtained. The cross-sectional image of the AlN template obtained by a scanning electron microscope (SEM, Hitachi S4800) is presented in Fig. 1(c). Obviously, the AlN epilayer with a measured thickness of 1.5 μm in the SEM image is well consistent with the structural design shown in Fig. 1(b). Fig. 1(d) and (e) presents the rocking curves of the AlN template obtained by a high-resolution X-ray diffractometer (HRXRD, Bruker D8), respectively. The full width at half maximum (FWHM) values for (0002) and (10$\bar{1}$2) planes are 80.5 and 565.9 arcsec, respectively. The FWHM values of (0002) and (10$\bar{1}$2) planes are commonly used to evaluate the dislocations in heteroepitaxial material. It is well known that a widened rocking curve corresponds to a larger FWHM value, which means a higher dislocation density [18]. The low FWHM values of the AlN template indicate its high crystalline quality. The peak in Fig. 1(d) is at $\theta = 18.015°$ with a deviation of about 0.1° from the standard value, indicating a little stress in the AlN template [19]. In Fig. 1(f), it shows the surface morphology image of the AlN template with a scan area of 10 × 10 μm obtained by an atomic force microscope (AFM, Veeco), which presents

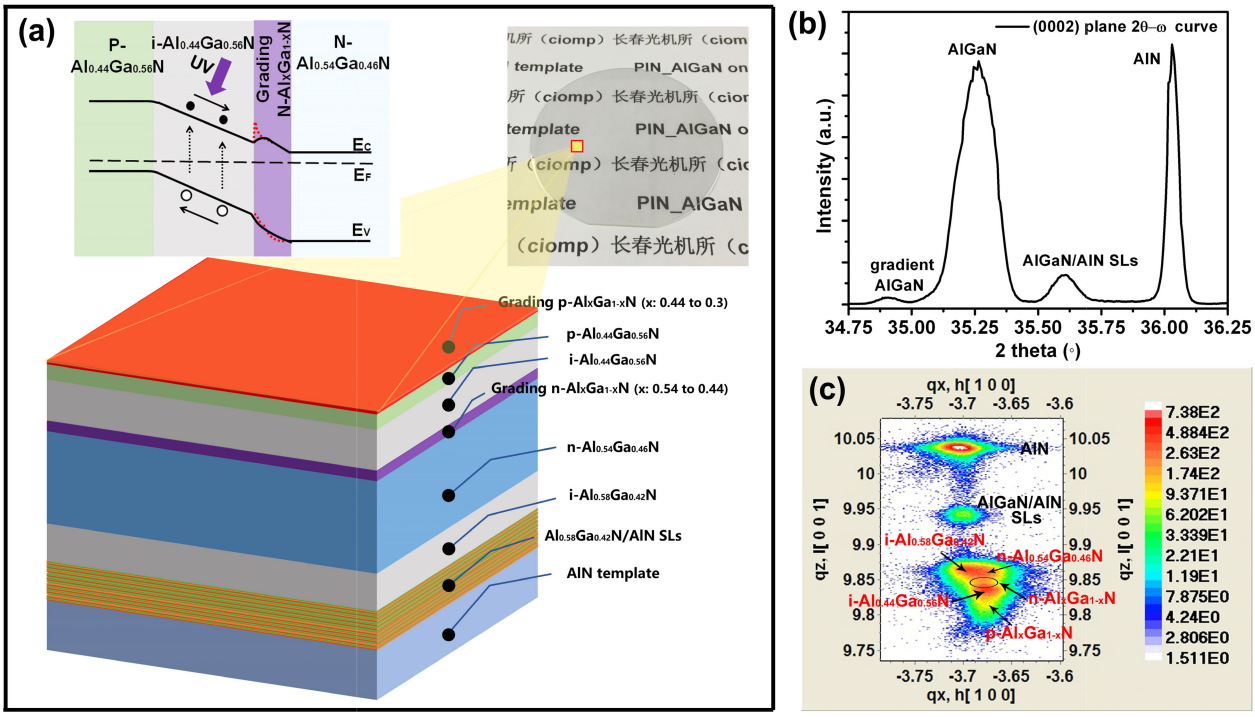

Fig. 2. (a) 2-in p-i-n structure AlGaN material and its corresponding structure and energy band diagram. (b) (0002)-plane 2θ-ω scanning curve. (c) Asymmetrical RSM around the (10$\bar{1}$5) reflection.

a smooth surface without any V-type pits or hillocks and a root mean square (rms) roughness of 0.856 nm. The above characterization results confirm the feasibility of using a thin MT-AlN interlayer and high-temperature AlN growth rate controlling method to obtain a high-quality AlN template for high Al content AlGaN growth.

Based on the pregrown AlN template, a polarization-enhanced p-i-n structure AlGaN-based solar-blind UV photodetector material is designed and prepared. The schematic of the device structure, the energy band diagram of the active layers, and its actuality is shown in Fig. 2(a) (inset). Differing from the conventional p-i-n structure, an n-$Al_xGa_{1-x}N$ grading layer with Al content gradually changing from 0.54 to 0.44 and a p-$Al_xGa_{1-x}N$ grading layer with Al content gradually changing from 0.44 to 0.3 are designed in our photodetector. Due to the nitriding treatment process during the growth of the AlN template, it realizes the N-face polar growth mode for the subsequent layers. For N-face polar growth along [1] direction, the Al content linearly changing from 0.54 to 0.44 in the n-$Al_xGa_{1-x}N$ grading layer will lead to a linear polarization change in it, resulting in a fixed positive space charge in the n-$Al_xGa_{1-x}N$ grading layer [17], [20]. The formed positive polarization charge field will attract the photon-generated electrons in the p-n junction and the bound sheet negative charges at the heterogeneous interface [21], [22]. The energy band diagram of the active layers reveals the effect of the introduction of n-$Al_xGa_{1-x}N$ grading layer on the i-$Al_{0.44}Ga_{0.56}N$/n-$Al_{0.54}Ga_{0.46}N$ heterogeneous interface. Due to the polarization regulation provided by the n-$Al_xGa_{1-x}N$ grading layer, the barrier of the heterogeneous interface is reduced, which is favorable for photogenerated electrons to pass through it and contribute photocurrent. Similarly, the Al content linearly changing from 0.44 to 0.3 in the p-$Al_xGa_{1-x}N$ grading layer will lead to a linear polarization change, resulting in a fixed negative space charge in it. The formed negative polarization charge field will attract the photon-generated holes in the p-n junction. Their combined effect improves the separation and transmission of the photon-generated electron-hole pairs so as to improve the performance of the AlGaN-based solar-blind UV photodetector. Following the structural design, the epitaxial growth is implemented on the pregrown AlN template. During the growth, TMAl, trimethylgallium (TMGa), and NH_3 are used as Al, Ga, and N precursors, while silane (SiH_4) and dicyclopentadienyl magnesium (Cp_2Mg) are used as n- and p-type dopants, respectively. Starting with the growth of a ten-period of $Al_{0.58}Ga_{0.42}N$/AlN (6/6 nm) superlattices (SLs) by periodically controlling the Ga source, it is used to release the strain accumulated by the heterogeneous mismatch in the subsequent films fabricated on the AlN template. An unintentionally doped $Al_{0.58}Ga_{0.42}N$ (i-$Al_{0.58}Ga_{0.42}N$) layer (200 nm) is then grown on top of the SLs. After the silicon doped n-type $Al_{0.54}Ga_{0.46}N$ (450 nm) window layer with a carrier concentration of 5.2×10^{18} cm^{-3} and an electron mobility of 13 $cm^2V^{-1}s^{-1}$ is deposited on the i-$Al_{0.58}Ga_{0.42}N$, an n-$Al_xGa_{1-x}N$ gradient layer (about 50 nm) with Al composition gradually reducing from 0.54 to 0.44 to eliminate band discontinuity and to form graded polarization is grown prior to the unintentionally doped $Al_{0.44}Ga_{0.56}N$ (i-$Al_{0.44}Ga_{0.56}N$) absorption layer (280 nm) that is used to reduce junction capacitance and increase sensitivity [23]. A magnesium doped p-$Al_{0.44}Ga_{0.56}N$ (80 nm) with a carrier concentration of 2.3×10^{17} cm^{-3} and a hole mobility of 3.9

$cm^2\ V^{-1}\ s^{-1}$ and a p-$Al_xGa_{1-x}N$ (20 nm) with Al composition gradually reducing from 0.44 to 0.3 are then grown on i-$Al_{0.44}Ga_{0.56}N$ absorption layer sequentially. It should be noted that, in addition to inducing the formation of a polarization field to improve the separation and transmission of photon-generated holes, this also makes the p-type doping efficient [24]. In addition, the p-$Al_xGa_{1-x}N$ is also beneficial to the electrode in order to form a good electrical contact.

To intuitively understand and evaluate the performance of polarization-enhanced p-i-n structure photodetector material, we characterize it using the HRXRD. Its typical 2θ-ω scanning curve of (0002)-plane is shown in Fig. 2(b). As can be seen, three main peaks are located at 36.03°, 35.6°, and 35.27°, respectively, corresponding to AlN, AlGaN/AlN SLs, and AlGaN. It should be noted that the AlGaN peak obtained by the symmetrical plane measurement is a combined peak of $Al_xGa_{1-x}N$ layers with different Al components, which can be distinguished from the asymmetrical reciprocal space mapping (RSM) image. The well-resolved RSM image of the structural material around $(10\bar{1}5)$ plane is presented in Fig. 2(c). The reciprocal lattice points (RLPs) mainly correspond to the AlN, AlGaN/AlN SLs, i-$Al_{0.58}Ga_{0.42}N$, n-$Al_{0.54}Ga_{0.46}N$, n-$Al_xGa_{1-x}N$, i-$Al_{0.44}Ga_{0.56}N$, p-$Al_{0.44}Ga_{0.56}N$, and p-$Al_xGa_{1-x}N$ layers, as illustrated in Fig. 2(c). The Al content fluctuation between i-$Al_{0.58}Ga_{0.42}N$ layer and n-$Al_{0.54}Ga_{0.46}N$ layer results in the expansion of the RLPs along the q_x direction. The region marked by a black circle is the RLPs corresponding to the n-$Al_xGa_{1-x}N$ gradient layer transitioning from the n-$Al_{0.54}Ga_{0.46}N$ layer to the i-$Al_{0.44}Ga_{0.56}N$ layer. This gradient layer not only eliminates the band discontinuity between the n-$Al_{0.54}Ga_{0.46}N$ layer and the i-$Al_{0.44}Ga_{0.56}N$ layer, but also introduces a linear change in the polarization, leading to a fixed positive space charge in it. The resulting positive charge field will benefit to attract the photon-generated electrons, which indirectly inhibits the photon-generated carriers' loss from reflection or trapping at the heterojunction [17].

B. Array Preparation

Developing small-size and large-array p-i-n structure detectors is the key to realizing AlGaN-based solar-blind UV FPA photosensors. After the epitaxial growth of the material, in order to eliminate the complexes generated by the combination of Mg atoms and H atoms during the reaction process and to increase the hole concentration of the p-type material, the obtained material is subjected to a rapid annealing process at 850 °C in a nitrogen (N_2) atmosphere to activate the Mg dopants. Subsequently, the array mesas and their electrodes are fabricated by standard optoelectronic processes, mainly plasma-enhanced chemical vapor deposition (PECVD), standard photolithography, inductively coupled plasma (ICP) etching, and e-beam evaporation. Taking a single pixel as an example, the detailed process steps are illustrated in Fig. 3(a), which mainly involves the following steps.

1) A SiO_2 mask layer is deposited on the surface of the p-i-n structure AlGaN-based solar-blind UV photodetector material by PECVD.

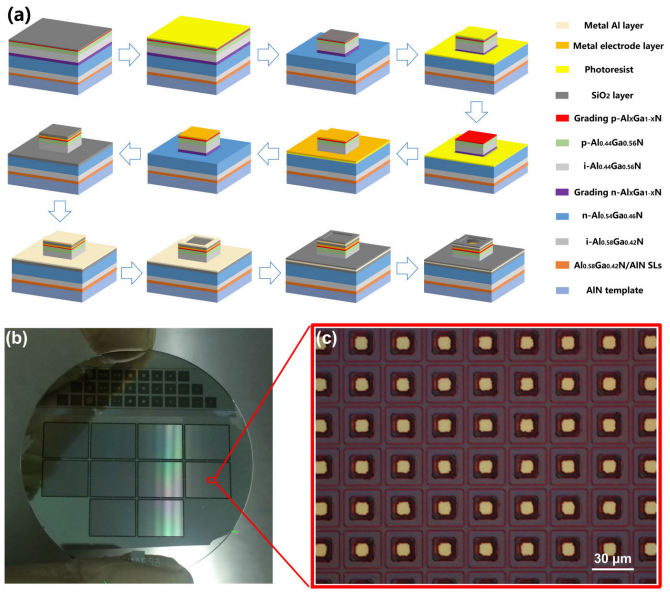

Fig. 3. (a) Array fabrication process flow diagram using a single pixel as an example. (b) p-i-n structure AlGaN photodetector arrays. (c) Partial enlargement of (b).

2) Spin-coating positive photoresist on the SiO_2 mask layer.
3) Supplemented by the standard photolithography process, the SiO_2 mask layer is etched by ICP, leaving a 26-μm^2 SiO_2 mask mesa. After removing the photoresist on it and etching to the n-$Al_{0.54}Ga_{0.46}N$ layer by ICP, a 26-μm^2 mesa of the photodetector is obtained.
4) After removing the SiO_2 mask mesa by ICP etching or wet etching, the negative photoresist is spin-coated on the surface of the patterned material.
5) Supplemented by the standard photolithography process, the negative photoresist on the photodetector mesa is removed.
6) The Ni/Au (10/300 nm) metal layers are deposited on the photodetector mesa by e-beam evaporation.
7) Using the lift-off process to leave Ni/Au metal layers (p-type electrode) on the photodetector mesa.
8) Depositing SiO_2 film on the surface of the patterned material by PECVD as an insulator layer.
9) Depositing Al (100 nm) metal layer on the surface of SiO_2 insulator layer.
10) Spin-coating positive photoresist on the surface of the Al metal layer. Supplemented by the standard photolithography process, the Al film is subsequently etched by ICP, exposing the SiO_2 insulator layer on the photodetector mesa.
11) Once again, depositing SiO_2 film on the surface of the patterned material by PECVD as a passivating layer to cover the patterned Al film.
12) Spin-coating positive photoresist on the surface of the SiO_2 passivating layer. Supplemented by the standard photolithography process, the SiO_2 insulator layer and the SiO_2 passivating layer are etched by ICP etching, leaving a circular hole on the mesa, which exposes the surface of the Ni/Au metal layer on the photodetector mesa.

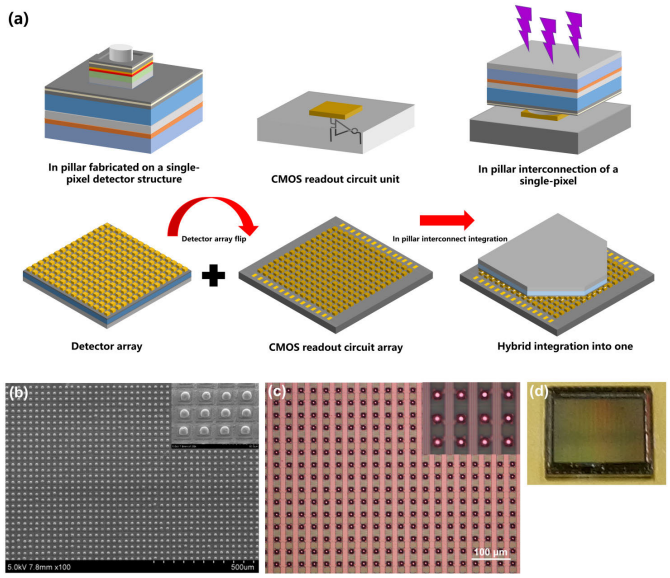

Fig. 4. (a) Detailed schematic of flip-chip bonding of detector array and CMOS readout circuit. (b) p-i-n AlGaN array with In bumps. (c) CMOS readout circuit array with In bumps. (d) Physical image of FPA photodetector.

After completing the steps mentioned above, the AlGaN-based self-powered solar-blind UV photosensor array with Al masking technology that is opaque to visible light is obtained. Then, using the same photolithography process and lift-off technique, a rectangular ring n-type electrode (Ti/Al/Ni/Au (30/100/30/300 nm) is fabricated at the outermost edge of the photodetector array. Finally, an indispensable step of rapidly annealing the sample at 700 °C for 1 min in a nitrogen atmosphere is carried out to obtain a good ohmic contact and improve the electrical properties. Fig. 3(b) and (c) shows the images of the fabricated p-i-n structure AlGaN-based photodetector arrays on the 2-in substrate and their partial enlargement, clearly presenting an array period of 30 μm and a pixel size of 26 $\times$ 26 μm^2.

III. Hybrid Integration of Detector Array and CMOS

Hybrid integration of the detector array and CMOS readout circuit is a crucial step in the practical application of AlGaN-based solar-blind UV focal plane detectors. Fig. 4(a) presents the illustration of flip-chip bonding of the detector array and the CMOS readout circuit. It should be noted that the commercial CMOS readout circuit model is ISC9809 (Indigo Systems, Inc.) with an array size of 320 $\times$ 256 and a pitch of 30 μm [25]. A capacitive transimpedance amplifier input circuit (CTIA) supplies a low-noise front end for each pixel. The sensor signal is integrated onto the CTIA feedback capacitor. The voltage on the integration capacitor is sampled and multiplexed to the column amplifier, thus realizing the sensor signal extraction [26]. Before flip-chip bonding, indium (In) bumps are fabricated by photolithography, thermal evaporation, and lift-off processes on the obtained array structure and CMOS readout circuit, which have good ductility and shear strength and can be welded at a lower temperature [27], [28]. The regional images and their enlarged details of the In bumps for both the photodetector array and the CMOS readout circuit are shown in Fig. 4(b) and (c), including their insets. As a supplementary note, the In bumps have undergone reflow treatment at 200 °C and were deoxidized with formic acid. The hybrid integration of the detector array and the CMOS readout circuit is carried out on the FC150 equipment with bonding conditions of chip and substrate temperatures at 160 °C, force of 400 N for 120 s. After hybrid integration, low-temperature epoxy resin is used to fill in the gap formed by In bumps and then be solidified. Finally, the physical 320 $\times$ 256 FPA AlGaN-based solar-blind UV photodetector obtained by the above processes is shown in Fig. 4(d).

IV. Testing and Functional Verification

Testing and functional verification are indispensable steps to confirm that the FPA photosensor is feasible and practical. This section will mainly perform electrical testing, spectral response testing, and deep UV imaging functional verification at room temperature, whose results have been plotted. Fig. 5(a) shows the typical I–V characteristic curve of a single photodetector in a dark environment, measured by a semiconductor parameter analyzer (Agilent B1500A). Due to the small pixel size, beryllium copper probes with tips of 5 μm are used in the measurement process. It presents a lower dark current of less than 10 nA at the reverse bias of 5 V. The I–V characteristic curve shows a typical diode rectification feature, and its ideality factor, rectification ratio, and specific ON-state resistance are evaluated to be about 1.55, 10^6, and 100 kΩ, respectively. In addition, the spectral response characteristics of a single pixel in the FPA photosensor, including responsivity and external quantum efficiency (EQE), are demonstrated in Fig. 5(b) and (c), respectively. Relevant data are obtained by a UV spectral response testing system using a 300-W xenon lamp as a light source and a UV-enhanced silicon-based photodetector as a calibration [2]. The FPA photodetector is enabled to be operated at zero-bias voltage with a response band between 262 and 281 nm, indicating its self-powered function, and has a responsivity of about 142 mA/W at the peak response of 271 nm, corresponding to a maximum EQE of 65.3%. The UV/visible rejection ratio ($R_{271\,\mathrm{nm}}/R_{400\,\mathrm{nm}}$) is more than four orders of magnitude. The transient spectral response at a reverse bias of 5 V is shown in Fig. 5(d). The measured rise time (τ_{rise}) from 10% to 90% of the peak value is about 7.807 ns, while the decay time (τ_{fall}) from 90% to 10% is 12.88 ns, which is stimulated by a tunable laser (Continuum, Horizon OPO) at 266 nm and recorded by a digital oscilloscope (Tektronix DPO 5104). Its fast transient response benefits from a reasonable structure that reduces the equivalent capacitance of the device. Compared with other published results as shown in Table I, it shows relatively good comprehensive performance, especially in the transient response speed. In Fig. 5(e) and (f), the sealed 320 $\times$ 256 solar-blind UV FPA photodetector and its functional verification result are shown, respectively. The imaging verification of the FPA photodetector is conducted under a simple condition, that is, the "UV" object is illuminated by commercial deep UV light-emitting diodes (LEDs) (λ = 275 nm), and its image is

TABLE I
PARAMETERS COMPARISON WITH REPORTED SOLAR-BLIND UV PHOTOSENSORS

Material	Peak wavelength (nm)	Structure of sensor	Rise time/Decay time	Dark current (A)	Responsivity (mA/W)	UV/Vis rejection ratio	I_{On}/I_{Off} ratio	Self-powered	Ref.
Semipolar AlGaN	~ 270	MSM	~ 90 ms/~ 720 ms	0.78×10^{-12} (10 V)	1842 (10 V)	-	$\sim 10^4$	Yes	[7]
Doped $MoS_2/SnSe_2$	254	Transistor	150 μs/234 μs	-	500	250	-	Yes	[11]
Graphene/$PtSe_2$ /β-Ga_2O_3	~ 240	Schottky	1.2 μs/503.4 μs	-	76.2 (0 V)	1.8×10^4	$\sim 10^5$	Yes	[29]
β-Ga_2O_3 nanowires	~ 258	Schottky	~ 1 μs/~ 60 μs	10^{-11} (-30 V)	2.9 (-50 V)	~ 38	-	Yes	[30]
$ZnGa_2O_4$/Si	~ 242	MIS	240 ms/120 ms (0.4 V)	10^{-8} (-5V)	7.5 (0 V)	~ 300	-	Yes	[31]
AlGaN/AlN	~ 240	Transistor	537.5 ps/3.1 μs	$\sim 1.7 \times 10^{-12}$ (-20 V)	1.6×10^7 (-20 V)	$\sim 10^3$	$\sim 10^8$	Yes	[32]
h-BN	~ 212	MS	~ 0.32 s/~ 0.63 s	2×10^{-11} (20 V)	0.1 (20 V)	-	$\sim 10^3$	No	[33]
AlGaN	~ 271	PIN	7.807 ns/12.88 ns	10^{-8} (-5V)	142 (0 V)	$\sim 10^4$	-	Yes	This work

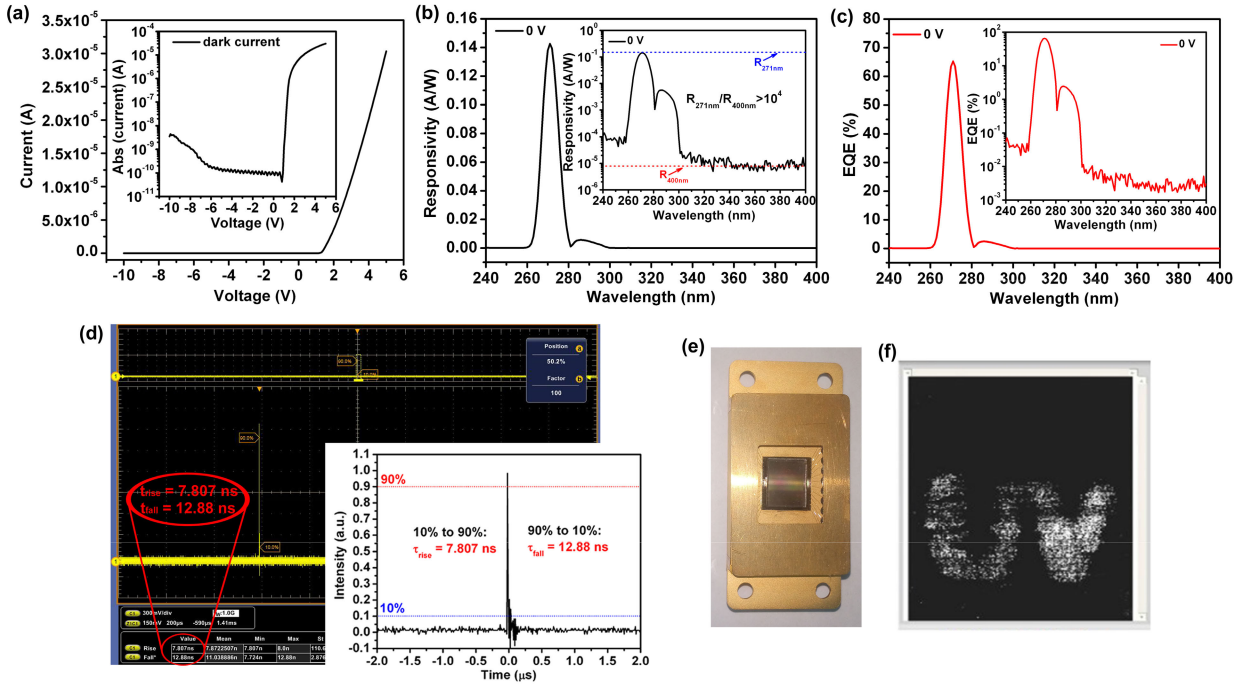

Fig. 5. (a) $I-V$ characteristic curve of a PFA photodetector pixel without illumination. (b) Spectral response. (c) Corresponding EQE of a single pixel in an FPA photodetector. (d) Transient spectral response at a reverse bias of 5 V. (e) Sealed AlGaN-based FPA photodetector. (f) Deep UV imaging photograph.

projected on the FPA photodetector through a single convex lens. It must be pointed out that imaging integrity needs to be improved by device process optimization.

V. CONCLUSION

A polarization-enhanced p-i-n structure photosensor material was grown on a specially regulated high-quality AlN template using MOCVD technology. The related HRXRD rocking curves, HRXRD asymmetric RSM, SEM imaging, and AFM imaging were plotted to evaluate the performance of the material. Then, after rapid annealing, standard optoelectronic processes such as PECVD, photolithography, ICP etching, and e-beam evaporation were used to fabricate a 320 × 256 FPA photosensor, which developed an Al masking technology that was opaque to visible light, enabling the FPA photosensor to achieve a high UV/visible rejection ratio ($R_{271\,\mathrm{nm}}/R_{400\,\mathrm{nm}} > 10^4$). Subsequently, the FPA and the commercial CMOS readout circuit were integrated by flip-chip welding through In bumps interconnection and sealed with low-temperature epoxy resin. The related optical and electrical performance tests were carried out on the as-prepared photosensor array. Its responsivity and EQE peaks operating at zero-bias voltage reached 142 mW/A and 65.3% at 271 nm, respectively, with a fast response speed ($\tau_{\mathrm{rise}} = 7.807$ ns and $\tau_{\mathrm{fall}} = 12.88$ ns) at a reverse bias of 5 V. In addition, its typical dark current was lower than 10 nA at a reverse bias of 5 V. The testing results and simple functional verification image confirmed the basic function of the FPA photosensor, which could be used in

solar-blind UV imaging. It should be noted that the detector performance, such as integrity, can be further improved by fabricating optimization.

ACKNOWLEDGMENT

The authors would like to thank Xiamen Future Display Technology Research Institute Company Ltd., Xiamen, China, for providing process guidance.

REFERENCES

[1] R. G. Safin, I. S. Gaĭnutdinov, R. S. Sabirov, and M. K. Azamatov, "Solar-blind filter for the ultraviolet region," *J. Opt. Technol.*, vol. 74, no. 3, pp. 208–210, 2007, doi: 10.1364/JOT.74.000208.

[2] Y. Chen, Z. Zhang, H. Jiang, Z. Li, G. Miao, and H. Song, "The optimized growth of AlN templates for back-illuminated AlGaN-based solar-blind ultraviolet photodetectors by MOCVD," *J. Mater. Chem. C*, vol. 6, no. 18, pp. 4936–4942, 2018, doi: 10.1039/c8tc00755a.

[3] Q. Cai et al., "Progress on AlGaN-based solar-blind ultraviolet photodetectors and focal plane arrays," *Light, Sci. Appl.*, vol. 10, no. 1, p. 94, Apr. 2021, doi: 10.1038/s41377-021-00527-4.

[4] T. Tut, T. Yelboga, E. Ulker, and E. Ozbay, "Solar-blind AlGaN-based *p–i–n* photodetectors with high breakdown voltage and detectivity," *Appl. Phys. Lett.*, vol. 92, no. 10, Mar. 2008, Art. no. 103502, doi: 10.1063/1.2895643.

[5] H. Srour et al., "Solar blind metal-semiconductor-metal ultraviolet photodetectors using quasi-alloy of BGaN/GaN superlattices," *Appl. Phys. Lett.*, vol. 99, no. 22, Nov. 2011, Art. no. 221101, doi: 10.1063/1.3662974.

[6] H. Ferhati, F. Djeffal, A. Saidi, A. Benhaya, and A. Bendjerad, "Effects of annealing process on the structural and photodetection properties of new thin-film solar-blind UV sensor based on Si-photonics technology," *Mater. Sci. Semicond. Process.*, vol. 121, Jan. 2021, Art. no. 105331, doi: 10.1016/j.mssp.2020.105331.

[7] Y. Gao et al., "Semipolar $(11\bar{2}2)$ AlGaN-based solar-blind ultraviolet photodetectors with fast response," *ACS Appl. Mater. Interface*, vol. 14, no. 18, pp. 21232–21241, Apr. 2022, doi: 10.1021/acsami.2c03636.

[8] Y. Chen, C. Zheng, and Y. Chen, "High-performance AlGaN-based solar-blind UV photodetectors for sensing applications," *Phys. Status Solidi, A*, vol. 218, no. 18, Sep. 2021, Art. no. 2100207, doi: 10.1002/pssa.202100207.

[9] N. Liu et al., "Fast-response amorphous Ga_2O_3 solar-blind ultraviolet photodetectors tuned by a polar AlN template," *IEEE Electron Device Lett.*, vol. 43, no. 1, pp. 68–71, Jan. 2022, doi: 10.1109/LED.2021.3132497.

[10] K. Benyahia, F. Djeffal, H. Ferhati, A. Bendjerad, A. Benhaya, and A. Saidi, "Self-powered photodetector with improved and broadband multispectral photoresponsivity based on ZnO-ZnS composite," *J. Alloys Compounds*, vol. 859, Apr. 2021, Art. no. 158242, doi: 10.1016/j.jallcom.2020.158242.

[11] Y. Yu et al., "Doping engineering in the $MoS_2/SnSe_2$ heterostructure toward high-rejection-ratio solar-blind UV photodetection," *Adv. Mater.*, vol. 34, no. 43, Oct. 2022, Art. no. 2206486, doi: 10.1002/adma.202206486.

[12] M. Long et al., "Ultrasensitive solar-blind ultraviolet photodetector based on $FePSe_3/MoS_2$ heterostructure response to 10.6 μm," *Adv. Funct. Mater.*, vol. 32, no. 34, Aug. 2022, Art. no. 2204230.

[13] H. Ferhati and F. Djeffal, "High-responsivity MSM solar-blind UV photodetector based on annealed ITO/Ag/ITO structure using RF sputtering," *IEEE Sensors J.*, vol. 19, no. 18, pp. 7942–7949, Sep. 2019, doi: 10.1109/JSEN.2019.2920815.

[14] H. P. T. Nguyen, "Graphene-driving novel strain relaxation towards AlN film and DUV photoelectronic devices," *Light, Sci. Appl.*, vol. 11, no. 1, p. 164, May 2022, doi: 10.1038/s41377-022-00861-1.

[15] Y. Chen et al., "Influence of the growth temperature of AlN nucleation layer on AlN template grown by high-temperature MOCVD," *Mater. Lett.*, vol. 114, pp. 26–28, Jan. 2014, doi: 10.1016/j.matlet.2013.09.096.

[16] N. Okada et al., "Investigation of off-cut angle of sapphire for epitaxial lateral overgrowth of AlN and fabrication of high-quality AlN template," *J. Cryst. Growth*, vol. 588, Jun. 2022, Art. no. 126640, doi: 10.1016/j.jcrysgro.2022.126640.

[17] Y. Chen, Z. Zhang, G. Miao, H. Jiang, Z. Li, and H. Song, "Epitaxial growth of polarization-graded AlGaN-based solar-blind ultraviolet photodetectors on pre-grown AlN templates," *Mater. Lett.*, vol. 281, Dec. 2020, Art. no. 128638, doi: 10.1016/j.matlet.2020.128638.

[18] M. Takeuchi et al., "Al- and N-polar AlN layers grown on *c*-plane sapphire substrates by modified flow-modulation MOCVD," *J. Cryst. Growth*, vol. 305, no. 2, pp. 360–365, Jul. 2007, doi: 10.1016/j.jcrysgro.2007.04.004.

[19] S. K. Jana et al., "High-resolution X-ray diffraction analysis of $Al_xGa_{1-x}N/In_xGa_{1-x}N/GaN$ on sapphire multilayer structures: Theoretical, simulations, and experimental observations," *J. Appl. Phys.*, vol. 115, no. 17, May 2014, Art. no. 174507, doi: 10.1063/1.4875382.

[20] A. Kalra, S. Rathkanthiwar, R. Muralidharan, S. Raghavan, and D. N. Nath, "Polarization-graded AlGaN solar-blind p-i-n detector with 92% zero-bias external quantum efficiency," *IEEE Photon. Technol. Lett.*, vol. 31, no. 15, pp. 1237–1240, Aug. 1, 2019, doi: 10.1109/LPT.2019.2923147.

[21] E. Matioli et al., "High-brightness polarized light-emitting diodes," *Light, Sci. Appl.*, vol. 1, no. 8, p. e22, Aug. 2012, doi: 10.1038/lsa.2012.22.

[22] J. Simon, V. Protasenko, C. Lian, H. Xing, and D. Jena, "Polarization-induced hole doping in wide–band-gap uniaxial semiconductor heterostructures," *Science*, vol. 327, no. 5961, pp. 60–64, Jan. 2010, doi: 10.1126/science.1183226.

[23] S. Li et al., "Polarization induced pn-junction without dopant in graded AlGaN coherently strained on GaN," *Appl. Phys. Lett.*, vol. 101, no. 12, Sep. 2012, Art. no. 122103, doi: 10.1063/1.4753993.

[24] Y.-J. Lee, Y.-C. Yao, and Z.-P. Yang, "Numerical analysis on polarization-induced doping III-nitride n-i-p solar cells," *IEEE Photon. J.*, vol. 7, no. 1, pp. 1–9, Feb. 2015, doi: 10.1109/JPHOT.2015.2392374.

[25] Indigo Systems, Inc. (2003). *ISC9809 320 × 256 Low Background ROIC*. [Online]. Available: http://www.indigosystems.com/product/roic/9809.html

[26] E. Cicek et al., "Crack-free AlGaN for solar-blind focal plane arrays through reduced area epitaxy," *Appl. Phys. Lett.*, vol. 102, no. 5, Feb. 2013, Art. no. 051102, doi: 10.1063/1.4790839.

[27] J. Day, J. Li, D. Y. C. Lie, C. Bradford, J. Y. Lin, and H. X. Jiang, "III-nitride full-scale high-resolution microdisplays," *Appl. Phys. Lett.*, vol. 99, no. 3, Jul. 2011, Art. no. 031116, doi: 10.1063/1.3615679.

[28] Z. Liu et al., "Micro-light-emitting diodes with quantum dots in display technology," *Light, Sci. Appl.*, vol. 9, no. 1, p. 83, May 2020, doi: 10.1038/s41377-020-0268-1.

[29] D. Wu et al., "Highly sensitive solar-blind deep ultraviolet photodetector based on graphene/$PtSe_2/\beta$-Ga_2O_3 2D/3D Schottky junction with ultrafast speed," *Nano Res.*, vol. 14, no. 6, pp. 1973–1979, Jun. 2021, doi: 10.1007/s12274-021-3346-7.

[30] X. Chen et al., "Self-powered solar-blind photodetector with fast response based on Au/β-Ga_2O_3 nanowires array film Schottky junction," *ACS Appl. Mater. Interface*, vol. 8, no. 6, pp. 4185–4191, Feb. 2016, doi: 10.1021/acsami.5b11956.

[31] D. Han et al., "Performance enhancement of a self-powered solar-blind UV photodetector based on $ZnGa_2O_4$/Si heterojunction via interface pyroelectric effect," *Appl. Phys. Lett.*, vol. 118, no. 25, Jun. 2021, Art. no. 251101, doi: 10.1063/5.0049747.

[32] J. Lu, Z. Lv, X. Qiu, S. Lai, and H. Jiang, "Ultrasensitive and high-speed AlGaN/AlN solar-blind ultraviolet photodetector: A full-channel-self-depleted phototransistor by a virtual photogate," *Photon. Res.*, vol. 10, no. 9, pp. 2229–2238, Sep. 2022, doi: 10.1364/PRJ.467689.

[33] H. Liu et al., "High-performance deep ultraviolet photodetectors based on few-layer hexagonal boron nitride," *Nanoscale*, vol. 10, no. 12, pp. 5559–5565, 2018, doi: 10.1039/C7NR09438H.